Features Advances to Automatically Find Images for Application to Clinical Decision Support

Authors:
Peng Guo[a],
R. Joe Stanley[a],
Soumya De[a],
Rodney Long[b],
Sameer Antani[b],
George R. Thoma[b],
Dina Demner-Fushman[b],
Sudhir Sornapudi[a]

Authors Note:

[a]Department of Electrical and Computer Engineering
Missouri University of Science and Technology
Rolla, MO 65409-0040

[b]Lister Hill National Center for Biomedical Communications
National Library of Medicine, National Institutes of Health, DHHS
Bethesda, MD 20894, USA

Corresponding Author:

Dr. R.J. Stanley
Department of Electrical and Computer Engineering
Missouri University of Science and Technology
127 Emerson Electric Co. Hall
301 W 16th St
Rolla, MO 65409-0040
Email: stanleyj@mst.edu
Telephone: 573-341-6896
Fax: 573-341-4532

ABSTRACT
Filtering through ever increasing sources of information to find relevant information for clinical decisions is a challenging task for clinicians. In biomedical publications, there are a variety of items that can provide evidence to aid the decision making process. One example is illustration image analysis and classification, which has been used to characterize and distinguish specific image modalities; this capability in turn has been used to assist in the evidence gathering process. This paper examines clinical decision support applications and extends previous research for illustration modality discrimination analysis.

Specifically, global, HSV histogram-based, and Gabor filter-based features are compared to histogram-based features for modality classification on a set of 12,056 images from 2004-2006 biomedical publication issues of *Radiology* and *RadioGraphics* that were manually annotated by modality (radiological, photo, etc.). Using a nearest neighbor classifier, average modality discrimination results were obtained as high as 99.98% using correlated features computed from Gabor filter spectral coefficients. These experimental results indicate that image features, particularly correlation-based features, can provide modality discrimination useful for clinical decision support applications.

1. Introduction

Clinical decision support (CDS) computer applications can potentially give healthcare professionals, patients, and researchers useful knowledge to improve healthcare and health related decisions. Considering the large and ever growing repositories of biomedical data, there is a demand for systems and tools to aid in finding useful information in biomedical publications, text databases, image databases, electronic health care records, clinical notes, and other sources, including full text, to support clinical decisions. The role of images in providing information for CDS is examined in this study, where an "image" can refer to visual materials in electronic healthcare records, databases, and articles in biomedical publications. Biomedical images include conventional images (MRI, CT, PET, for example), as well as illustrations, charts, and graphs. By moving beyond conventional text-based searching to combining both text and image features ("visual features") in search queries, the overall research goal is to enhance information retrieval from these entities for clinical decision support. The approach and the tools investigated take advantage of advances in Information Retrieval (IR), Content-based Image Retrieval (CBIR), and Natural Language Processing (NLP).

This research has focused on improving information retrieval of visual content from biomedical publications, in particular, by using features of the images themselves in combination with cues from text associated with the images. This includes using text from figure captions, image modality information from visual features and accompanying text [1][2][3], and annotation markers, such as arrows [4], letters or symbols embedded in images [2].

From the CDS perspective, knowing and differentiating image modality can impact an image's utility and improve the relevance of query results. Some previous document retrieval work has used the UMLS [5] term and concept query expansion engine in combination with fields from search results such as MEDLINE®

citations (e.g., titles, abstracts and MeSH terms) and image features. This combination of attributes has been used to develop "visual keywords" with the goal of approximating image semantic labels [6][7]. Automatic illustration identification has been explored for illustrations in medical publications which may assist a clinician in determining the usefulness of a particular publication for patient monitoring and treatment [1][8][9][10].

A number of image features and techniques potentially useful for CDS have been applied in the field of Content-Based Image Retrieval (CBIR), including: 1) features of color, shape, and texture, and distance measures to compute similarity between images [9][10][11][12][20]; 2) Hough transform shape detection for region of interest determination and segmentation (has been used for lung images) [10]; 3) color analysis of stains for region of interest labeling (has been used for malaria cell images) [13]; 4) connecting the user and the database through a search engine with a feedback neural network architecture [14]; 5) query system modeling human interaction [15]; 6) Big Data use with query forms [16]; 7) use of image "key points" to identify salient parts of an image [17]; 7) combining image and text information for matrix similarity assessment [18]; 8) three-dimensional image analysis [8]; 9) latent topic models for computing image similarity [19]; 10) statistical model-based image feature extraction using the wavelet domain and a Kullback divergence-based similarity measure for CBIR [21]; and 11) localized texture characterizations for CBIR for remote sensing applications [22].

There have also been numerous studies which explore the use of text information for CDS applications, including: 1) extreme learning machine (ELM) and online sequential extreme learning machine (OSELM) with cuckoo search [23]; 2) cluster-based external expansion modelling with feedback [24]; 3) processing patient health record databases for matching, retrieval, and identification using templates for similarity assessments [25][26][27][28][29]; 4) graph theory and neural networks for literature mining [30]; 5) hash-based similarity searching

[31]; 6) fusion of image descriptors and text for medical image retrieval [32]; 7) automatically supplementing references with images from articles for evidence finding [33]; 8) demonstrating that image and text can yield retrieval accuracy appropriate for clinical evidence [34].

Recent publications related to the use of biomedical images in clinical decision support include: 1) an overview by Agarwal [35] of the critical steps of computer-assisted detection (CAD) and computer-assisted diagnosis (CADx) systems: preprocessing, segmentation, region of interest (ROI) analysis, and assessment of detected structures and linear discriminant analysis (LDA) and support vector machine (SVM) approaches for these types of classification applications; 2) the use of image capture with mobile phone camera technology for cervical cancer screening in low resource parts of Africa [36]; and 3) an approach for vertebral level localization in spine radiographs as decision support for target localization in spine surgery [37].

This study builds off of research related to biomedical image retrieval in the literature or related to image classification expected to be useful as preprocessing in clinical decision support systems, including: 1) automatic classification in a hierarchical taxonomy of figures from the biomedical literature [38]; 2) creating a comprehensive "visual ontology" for images in the biomedical literature [39]; 3) image modality classification, separation of compound figures, and image retrieval using the 2013 ImageCLEF image set [40] (see [41] for an overview of the results of all ImageCLEF biomedical image retrieval tasks 2004-2013); 4) biomedical image modality classification using image clustering with respect to specified features, expert labeling of the (relatively few) clusters, and image classification based on the cluster labels [42]; 5) modality classification of biomedical literature figures comparing the effectiveness of SVM classification using hand-crafted features versus a deep learning classifier [43]; 6) extracting endoscopic images from the biomedical literature [44] and distinguishing true

endoscopic images from confounding images; 7) classification of radiological signs in abdominal CT images [45]; 8) classification of view (frontal or lateral) in chest X-ray images [46]; 9) classification of Visible Human biomedical images into body segment classes (head and neck, thorax, abdomen, pelvis, and lower limb) by image features [47]; 10) methods to exploit "pointers" (such as arrows) or labels (such as letters or numbers) embedded within biomedical images, for image analysis and retrieval [48]; 11) the use of text associated with biomedical images to enhance image modality classification [49] and retrieval [50][51]; and 12) modality-based classification over a set of 742 images manually annotated by modality (such as radiological or photo) selected from the 2004-2005 issues of the *British Journal of Oral and Maxillofacial Surgery* using global, histogram-based, texture image illustration features, and basis function luminance histogram correlation features computed from the annotated images [1].

In this paper, a CDS application is presented that extends the image feature development work from [1]. Basis function features created from the HSV histogram and Gabor filter are compared to correlation features computed from the luminance histogram. . These quantities are applied to a set of medical publication illustrations and modalities examined in previous research [33]. The remainder of the paper is organized as follows: 1) description of the features and feature groups investigated, 2) modality classification experiments performed, 3) results and discussion, and 4) conclusions.

2. Methodology
2.1 Data Set Examined
In this study, images in various modalities were examined from the ImageCLEFMed 2010 dataset [52] from 2004-2006 issues of *Radiology* and *RadioGraphics* biomedical publications; these images were previously investigated by Demner-Fushman et al. in [33] for feature development and classification. Table 1 provides a description of the categories of truthed images in this dataset. From Table 1, there are 2470 positive id images for all of the categories and 9586 negative id images for all of

the categories. Positive id images represent truthed images in the designated categories. Negative id images are images from other categories that are similar to the designated categories for comparison. Figure 1 presents an image example from each of the category numbers listed in Table 1.

Table 1. Categories for Image Modality [4]

| Category Label	No. Positive Id Images	No. Negative Id Images
Doppler ultrasound images	286	513
CT images with emphysema	68	860
knee x-ray images	112	786
mediastinal CT	291	571
abdominal CT images showing liver blood vessels	299	721
chest CT images showing micro nodules	59	697
x-ray images containing one or more fractures	105	727
CT liver abscess	59	775
MRI or CT of colonoscopy	236	601
photographs of tumours	320	640
images of muscle cells	79	778
images containing a Budd-Chiari malformation	74	708
gastrointestinal neoplasm	273	607
pulmonary embolism all modalities	209	602
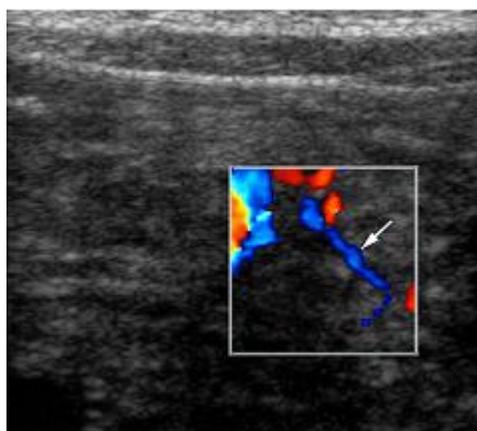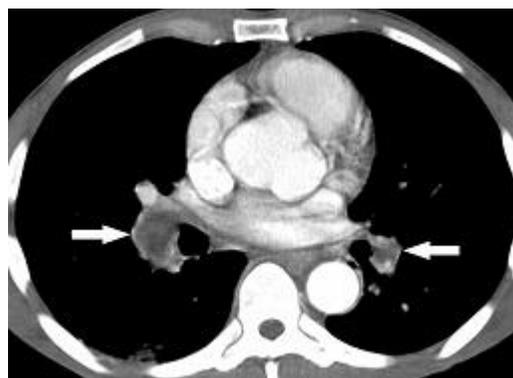


(a)   (b)

(c)
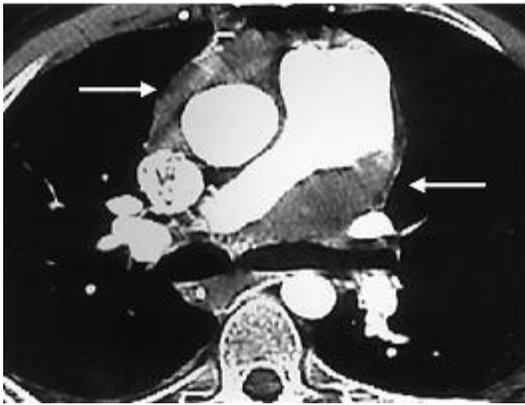
(d)

(e)
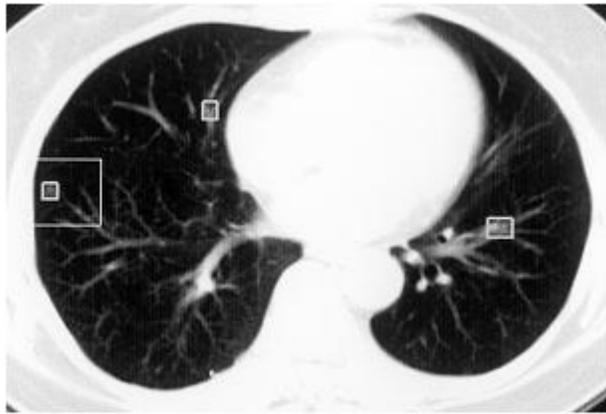
(f)

(g)
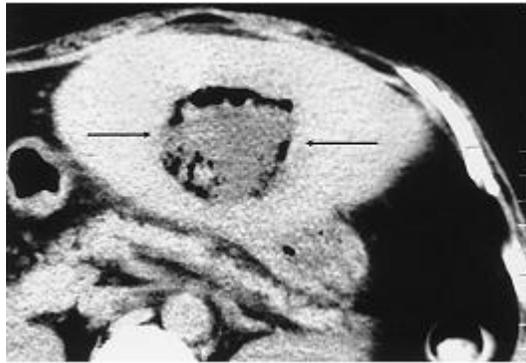
(h)
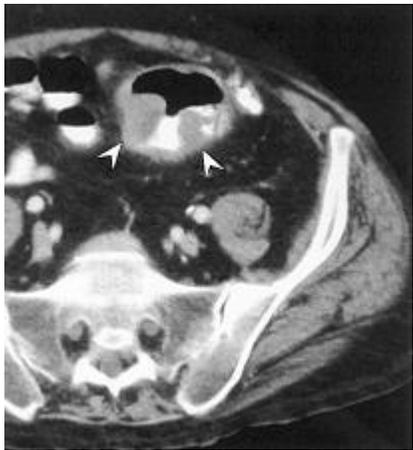
(i)
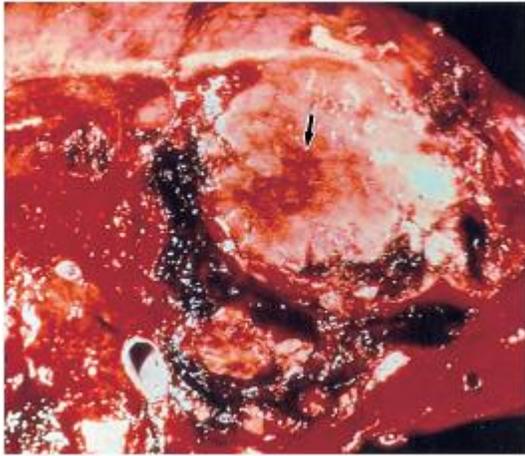
(j)
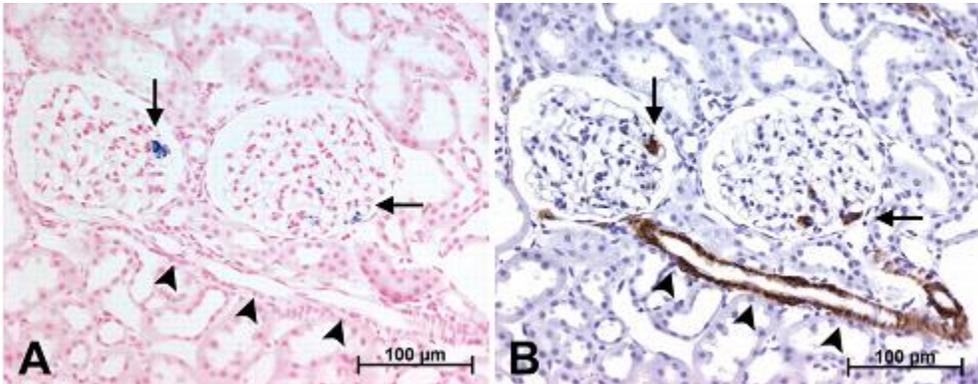
(k)
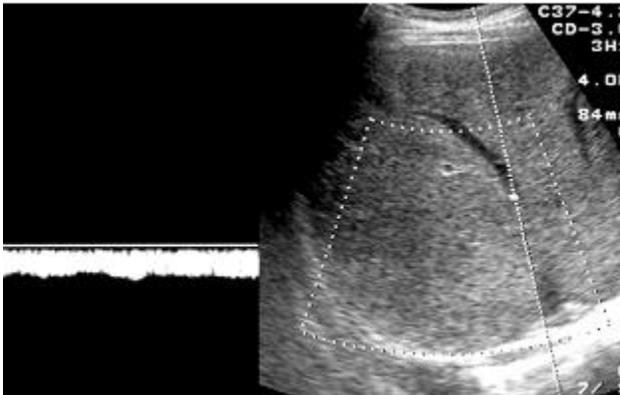
(l)
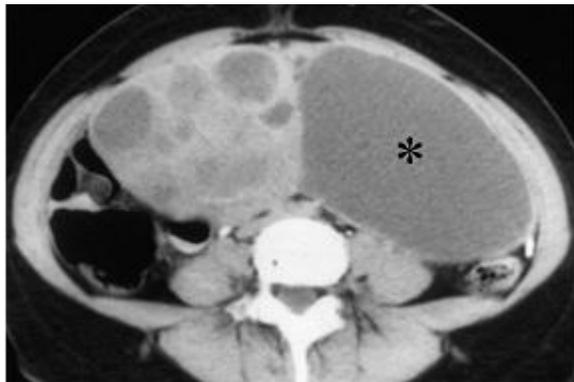
(m)

(n)

Figure 1: Image examples (positive id) from each of the category numbers listed in Table 1. (a) Doppler ultrasound image (reproduced with permission [53]). (b) CT image with emphysema (reproduced with permission [54]). (c) Knee x-ray image (reproduced with permission [55]). (d) Mediastinal CT image (reproduced with permission [56]). (e) Abdominal CT image showing liver blood vessels (reproduced with permission [57]). (f) Chest CT image showing micro nodules (reproduced with permission [58]). (g) X-ray image containing one or more fractures (reproduced with permission [59]). (h) CT liver abscess (reproduced with permission [60]). (i) MRI or CT of colonoscopy (reproduced with permission [61]). (j) Photograph of tumor (reproduced with permission [62]). (k) Image of muscle cells (reproduced with permission [63]). (l) Image containing a Budd-Chiari malformation (reproduced with permission [64]). (m) Gastrointestinal neoplasm (reproduced with permission [65]). (n) Pulmonary embolism all modalities (reproduced with permission [66]).

2.2 Features and Feature Groups Investigated
In prior research [1], the method of correlating basis functions with the luminance histogram for an image was found to be effective for discriminating image modalities [4]. These basis function correlation features have been explored in dermatology imaging research to provide gray level distribution information for skin lesion discrimination [67]. In this study, the basis function correlation features are extended to include the HSV histogram, both smoothed and unsmoothed, and Gabor features, denoted as Groups 1, 2, and 3, respectively. The details for these feature calculations are presented in the following sections.

2.2.1 HSV Histogram Correlation Features

Group 1 and Group 2 features are computed from unsmoothed, and smoothed, one-dimensional HSV histograms, respectively [20]. These features are computed as follows. Each pixel in the image contributes to the histogram weighted values of its hue 'H' and intensity 'V', based on its saturation 'S'. Hence, the histogram has two components, the color components representing the contribution of hue from each pixel, and the 'gray component', representing the contribution of the intensity value at each pixel. The histogram retains the smoothness between the adjacent components and this allows us to perform a window based smoothing of the histogram.

"Saturation projection" is used to determine the weights for hue and for intensity. The weight is dependent on saturation level s. The weight of hue component, $w_h(s)$ and the weight of

intensity of component $w_i(s)$ are computed using the equations [20]:

$$w_h(s) = s^r \text{ where } r \in [0,1] \qquad (1)$$

$$w_i(s) = 1 - w_h(s) \qquad (2)$$

The number of bins in the histogram is determined. Since the histogram consists of two components, the total number of bins is found by summing the number of color component bins and the number of gray component bins. Let N_h , N_g be the number of bins for the color and gray components, respectively, and let N be the total number of bins in the histogram [20]. Then

$$N_h = Round(2\pi MULT\_FCTR) + 1 \qquad (3)$$

$$N_g = Round(I_{max} / DIV\_FCTR) + 1 \qquad (4)$$

$$N = N_h + N_g \qquad (5)$$

where: $MULT\_FCTR$: is the multiplying factor that determines the quantization level for the hues.

I_{max} : is the maximum intensity (generally 255).

DIV_FCTR : is a division factor that determines the number of quantized gray levels.

The algorithm for generating the HSV histogram, denoted as *Hist*, is shown in Table 2 [20]:

Table 2. Algorithm for generating HSV histogram.

For each pixel in image:

    Convert RGB values to HSV

Update histogram as follows:

    $Hist[Round(H.MULT\_FCTR)] = Hist[Round(H.MULT\_FCTR)] + w_h(s)$

    $Hist[Round(2\pi MULT\_FCTR) + ROUND(V / DIV\_FCTR)]$
    $= Hist[Round(2\pi MULT\_FCTR) + ROUND(V / DIV\_FCTR)] + w_i(s)$

Traditional histograms do not provide perceptual gradation of colors, but the HSV histogram retains this property. Thus, image-based features are explored based on the smoothed and unsmoothed histograms. The smoothing operation for the HSV histogram is given using the following equation [20]:

$$Hist_w(j) = \sum_{i=j-N}^{j+N} w(i-j)Hist(i) \qquad (6)$$

where:

$$j \in [0, N_h + N_g - 1] \text{ and}$$

$$w(i-j) = 2^{-|i-j|}$$

For the image HSV histogram, let $Hist_U$ and $Hist_S$ denote the unsmoothed and smoothed histograms, respectively. The basis function correlation features with the unsmoothed and smoothed HSV histograms are defined as follows. The basis function weighted density distribution (WDD) functions are given in Figure 2 below.

(a)   (b)   (c)

(d)   (e)   (f)
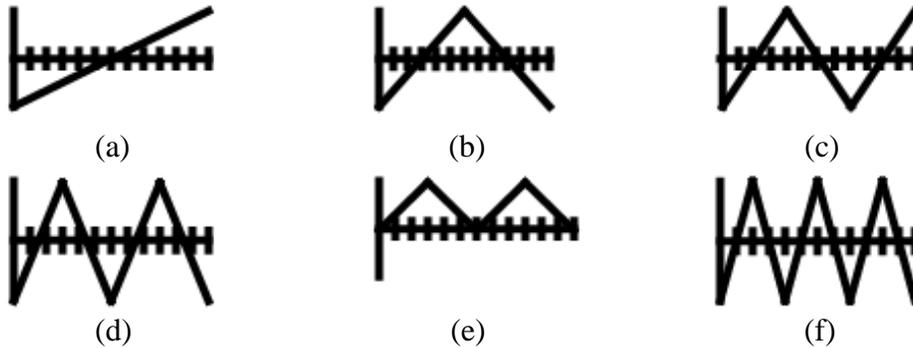
Figure 2. The WDD functions used for computing correlation-based features with the HSV unsmoothed and smoothed histograms and the Gabor filter coefficients (reproduced with permission [67]).

The basis function WDD correlation features for a given image for unsmoothed HSV histogram are computed as:

$$h_{Hist_U,k} = \sum_{i=1}^{N} Hist_U(i)W_k(i) \text{ for k = 1, 2, ..., 6} \qquad (7)$$

$$h_{Hist_U,k} = \sum_{i=1}^{N} |Hist_U(i) - Hist_U(i-1)|W_k(i) \text{ for k = 7, 8, ..., 12,} \qquad (8)$$

where $Hist_U(0) = 0$

The basis function WDD correlation features for the smoothed HSV histogram are similarly defined.

For each image, fifteen features are computed for the unsmoothed (Group 1) and smoothed (Group 2) HSV histograms. These features are: 1) the bin number which has the maximum

count (mostFrequentComponent), 2) the average value of the color and of the gray components in the image (avgVal), 3) the standard deviation of the color and of the gray components in the image HSV histogram (stdVal), 4) 12 basis function features, denoted as $h_{HistU,1}$-$h_{HistU,12}$ for the unsmoothed HSV histogram features and $h_{HistS,1}$-$h_{HistS,12}$ for the smoothed HSV histogram features.

2.2.2 Group 3
The final set of features explored are based on Gabor filters. Gabor filters have been applied in CBIR for purposes such as extracting text regions from document images [68] and for texture analysis [12] [69]. The Gabor features are computed from an image using the following procedure. First, the image is resized to a square of dimensions min_dim x min_dim, where

min_dim is the minimum of the row and column dimensions for the image. For example, a 512x768 image is resized to a 512x512 image. Second, if the image is color, it is normalized by applying a local luminance variance. Otherwise, the existing grayscale image is used. Third, the Gabor filter algorithm is applied to the resized image. The Gabor filter algorithm was used from [70] which is based on the algorithm presented in [71]. This algorithm uses orientations determined empirically at each scale of 8, 8, 4. Third, the array of spectral coefficients determined from the Gabor filter, denoted as I_{spect}, are correlated with the WDD basis functions to provide a profile of the spectral content and, thereby, texture information contained within the image. The WDD correlation features for a given image are defined as:

$$f_{I_{spect},k} = \sum_{i=1}^{192} I_{spect}(i)W_k(i) \quad \text{for k = 1, 2, ..., 6} \tag{9}$$

$$f_{I_{spect},k} = \sum_{i=1}^{192} \left| I_{spect}(i) - I_{spect}(i-1) \right| W_k(i) \text{ for k = 7, 8, ..., 12,} \tag{10}$$

where $I_{spect}(0) = 0$ and 192 spectral coefficients found from the Gabor filter.

3. Experiments Performed
A benchmark technique based on different image features from [1] was used in order to evaluate these basis function-based feature groups (Group1-Group 3). These features are summarized in section 3.1. Two modality classification experiments were performed based on the positive and negative ID images within each of the 14 categories given in Table 1. In the first experiment, twenty randomly generated training and test sets were used for a nearest neighbor classifier (radial clustering algorithm with zero distance parameter, making it a nearest neighbor classifier) developed in [1]. Each training set consists of 90% of the image data feature vectors for each category, and each corresponding test set contains the remaining 10% of the image data feature vectors for each category. The image data feature vectors include the features computed from Groups 1-3 and the benchmark features (see section 3.1)

from [1]. In the second classification experiment, an image was classified into one of the 14 categories using the dataset for the positive id images within each category. Twenty randomly generated training and test sets were used. The training set consisted of 90% of the positive id images for each category, with the test set containing the remaining 10% of the positive id images for each category.

3.1 Benchmark Features
For image-based modality discrimination in [1], developed features were organized into three categories, as follows: 1) General Features, 2) Basis Function Features, and 3) Texture Features. The General Features quantified color, grayscale, histogram, and topology differences for grayscale and color figures. The General Features included: 1-3) standard deviation of

red, green and blue values within the image, 4) percentage of the pixels in the image in which the green value is less than the red value and the green value is less than the blue value, 5) ratio of the pixels in the image with luminance value greater than or equal to 250, 6) ratio of the number of pixels with the most frequently occurring luminance value to the area of the image, 7) square root of the area of the image, 8) ratio of the sum of the absolute differences between the red and green values and the red and blue values for each pixel in the image to the area of the image, 9) ratio of the pixels in the image with luminance value less than or equal to 30, 10) square root of the number of luminance histogram bins with counts greater than or equal to the scaled area of the image, 11) square root of the number of luminance histogram bins with counts greater than 0, 12) the square root of the number of luminance histogram bins with counts greater than or equal the scaled area of the image, and 13) estimate of the image fractal dimension. The Basis Function Features were the twelve WDD features computed from the image luminance histogram. The Texture Features were texture measures based on the Generalized Gray Level Spatial Dependence Models for Texture.

3.2 Nearest Neighbor Classifier
The nearest neighbor classifier was used as follows for the two experiments. For the first experiment, the minimum Euclidean distance for each test image was found for each positive and for each negative image in the training set, for each classification category. The test image feature vector is labeled a positive image for the category if the Euclidean distance to the minimum positive image is less than the Euclidean distance to the minimum negative image. Otherwise, the test image is labeled a negative image. These steps were applied to classifying each test image based on the feature vectors determined for each of the 14 categories given in Table 1, over 20 training and test sets. The average test results are reported over these 20 trials. For the second experiment, the

minimum Euclidean distance was computed from each test image to each positive image in the training set, for all of the classification categories. The test image feature vector is assigned to the category of the positive image with the minimum Euclidean distance. These steps were applied to classifying each test image based on the feature vectors found from all of the categories given in Table 1 over 20 training and test sets. The average and standard deviation classification results were reported over these 20 trials.

4. Experimental Results and Discussion
The experiments performed evaluated the modality discrimination capability of the proposed image-based features computed by correlating the basis functions (see Figure 2) with the unsmoothed HSV histogram (Group 1), smoothed HSV histogram (Group 2), and the Gabor filter spectral coefficient array (Group 3). Classification results using these feature groups are compared to benchmark color, grayscale, histogram, and topology features (General Features), basis function correlation features with the luminance histogram (Basis Function Features) and the Generalized Gray Level Spatial Dependence Models for Texture Features (Texture Features) from [1]. Modality classification experiments were performed on the 2470 positive id and 9586 negative id images for all fourteen modality categories shown in Table 1. Table 3 presents the test results using the nearest neighbor classifier for feature Groups 1-3 and the General Features, Basis Function Features, and Texture Features benchmarks from [1]. The test results for each of the 20 randomly generated training/test sets are given with the mean and standard deviation for the respective feature groups. Table 4 presents the average positive and negative nearest neighbor test classification results over 20 randomly generated training and test sets for all 14 categories (multi-class) for feature Groups 1-3 and the General Features, Basis Function Features, and Texture Features benchmarks from [1].

Features Advances to Automatically Find Images for Application to Clinical Decision Support

Table 3. Average test results using the nearest neighbor classifier for feature Groups 1-3 and benchmark features [4] for 20 training/test sets.

Category	General Features [1]	Basis Function Features [1]	Texture Features [1]	Group 1	Group 2	Group 3
Doppler ultrasound images	91.13	99.75	96.75	99.88	84.50	99.88
CT images with emphysema	98.01	99.19	99.78	99.30	92.58	100.00
knee x-ray images	96.72	99.28	99.67	99.33	90.94	100.00
mediastinal CT	97.67	98.20	98.78	99.88	86.34	100.00
abdominal CT images showing liver blood vessels	90.83	99.95	99.12	99.51	86.62	100.00
chest CT images showing micro nodules	97.37	99.87	99.54	99.87	92.24	100.00
x-ray images containing one or more fractures	97.17	96.27	99.88	99.22	89.58	100.00
CT liver abscess	98.86	99.46	99.94	99.82	95.48	100.00
MRI or CT of colonoscopy	83.45	99.29	96.07	98.15	85.89	100.00
photographs of tumours	76.98	99.27	99.32	99.84	69.74	100.00
images of muscle cells	89.94	99.19	99.48	99.71	93.14	100.00
images containing a Budd-Chiari malformation	96.47	99.81	99.04	99.94	94.81	99.94
gastrointestinal neoplasm	72.90	94.66	80.68	91.36	74.49	99.83
pulmonary embolism all modalities	77.16	97.04	82.65	99.26	75.68	100.00
Average over all modality categories	90.33	98.66	96.48	98.93	86.57	99.98

Table 4. Multi-category test percentage correct results using nearest neighbor classifier for feature Groups 1-3 and benchmark features [4] for 20 training/test sets are presented with mean and standard deviation.

Training/ Test Set	General Features [1]	Basis Function Features [1]	Texture Features [1]	Group 1	Group 2	Group 3
1	75.71	93.93	88.26	94.74	90.69	98.79
2	77.33	95.14	91.50	95.14	93.12	98.79
3	83.00	94.74	91.50	94.74	92.31	99.19
4	77.33	91.09	87.45	92.31	91.90	98.79
5	74.49	93.12	87.45	94.33	90.28	97.57
6	76.52	91.90	89.88	92.31	91.09	97.98
7	76.11	94.33	89.88	93.52	93.52	99.19
8	70.04	91.90	89.07	93.12	88.26	98.38
9	76.52	95.14	90.69	93.93	91.90	98.38
10	70.04	89.47	87.04	91.50	89.07	98.79
11	77.73	95.14	89.47	91.50	90.69	97.57
12	77.33	93.93	92.31	89.88	92.31	99.60
13	74.49	90.69	90.69	93.52	90.69	99.19
14	70.85	89.07	87.85	95.55	92.31	99.60
15	75.71	92.71	89.88	94.33	92.31	98.79
16	75.30	91.50	89.07	95.55	94.33	98.38
17	74.49	91.50	89.47	96.36	91.09	99.60
18	73.68	93.12	89.07	93.93	89.07	98.79
19	76.52	90.28	89.88	96.76	92.71	98.38
20	78.14	91.90	89.07	93.52	91.09	100.00
Mean	75.57	92.53	89.47	93.83	91.44	98.79
Standard Deviation	2.98	1.90	1.43	1.73	1.54	0.66

From Tables 3 and 4, there are several observations. First, from Table 3, all of the feature groups provided the capability to effectively distinguish the positive labeled images from the negative labeled images for each category. Second, from Table 3, the WDD-based features in feature groups Groups 1-3 and Basis Function Features [1] yielded slightly higher average classification rates than the other feature groups, which are based on global image and texture features. In these feature groups WDD correlation-based features were computed using the luminance image (Basis Function Features [1]), the HSV space (with and without HSV histogram smoothing (Groups 1 and 2, respectively)), and with the Gabor filter coefficients (Group 3). Group 1 features based on correlating the basis functions with unsmoothed HSV histogram (98.93%) outperformed the Group 2 features based on correlating the basis functions with the smoothed HSV histogram (86.57%). Overall, the basis function features based on correlating the WDD functions with the Gabor filter spectral coefficients yielded the highest modality classification results, with an average of 99.98% over the 14 different categories. This is a slight improvement of 1.32% over correlating the WDD functions with the luminance histogram (Basis Function Features [1]). Third, from Table 4, the WDD correlation-based features yielded the highest overall multi-category

discrimination results. The Group 3 features, computed based on correlating the spectral coefficients from Gabor filtering with the WDD functions, produced the highest average classification results of 98.79%. These results and the other relatively high classification results based on the WDD correlation-based features, Basis Function Features [1] based on the luminance histogram (92.53%) and Group 1 based on the unsmoothed HSV histogram (93.83%) may indicate there is discrimination information in the distribution of gray levels and HSV values as well as the spectral coefficients over the images from the different categories in this data set. In the published literature, the WDD correlation-based features have been applied to extract symmetry and distribution information from histograms of malignant melanoma labeled colors for skin lesion discrimination [67]. This research appears to show another potential application for these basis function features in extracting distribution-based information which is similar for images of the different database categories. The nearest neighbor classifier results presented here highlight the similarity of images within each category using image-to-image matching. Fourth, the experimental results show that the General Features (global color and luminance features) from [1] and texture-based features (Generalized Gray Level Spatial Dependence Models) from [1] provided the lowest discrimination information for multi-category classification, with average test results of 75.57% and 89.47%, respectively. In the context of CDS applications, the image-based features presented in this study, particularly the basis function features from Group 3 which correlate the array of Gabor filter spectral coefficients with the WDD functions can be used to discern image modalities that are representative of different types of biomedical information.

4. Conclusion

In this research, modality image classification was investigated using feature groups generated from HSV histograms and Gabor filters, and showed that these features provide discrimination: capability for positive/negative classification. For selected modality categories, the classification results show the potential for using image feature-based and machine learning classification in clinical decision support. Overall, the correlated WDD features with the spectral coefficients determined from the Gabor filtering achieved average classification as high as 99.98% for the experimental data set. The modality classification results of 98.93% obtained by correlating the WDD basis functions with the unsmoothed HSV histogram outperforms the feature groups from previous research [1]. Future research can be focused on principal feature analysis and finding the most significant features, and in down-sizing the current feature groups.

As an initial step in characterizing the visual content for biomedical information retrieval systems, positive results were achieved in image modality classification, and have improved on previous research.

5. Acknowledgment

6. References

[1]   Stanley RJ, De S, Demner-Fushman D, Antani S, Thoma GR. An Image Feature-Based Approach to Automatically Find Images for Application to Clinical Decision Support. Comput. Med. Imaging Graph. 2011;35(5):365-372.

[2] De S, Stanley RJ, Cheng B, Antani S, Long R, Thoma G. Automatic Text Detection and Recognition in Annotated Biomedical Publication Images. International Journal of Healthcare Information Systems and Informatics (IJHISI). 2014;9(2):34-63.

[3]   Cheng B, Stanley RJ, De S, Antani S, Thoma GR. Automatic Detection of Arrow Annotation Overlays in Biomedical Images. International Journal of Healthcare Information Systems and Informatics (IJHISI). 2011;6(4):23-41.

[4]   Cheng B, Wang R, Antani S, Stanley RJ, Thoma GR. Graphical Image Classification Using a Hybrid of Combining an Evolutionary Algorithm and Binary Particle Swarm Optimization. Proc. 24th Annual Symposium on Electronic Imaging, Document Recognition and Retrieval XIX, San Francisco, CA. January 2012: vol. 8297, pp. 1-8.

[5]   Lindberg DA, Humphreys BL, McCray AT. The Unified Medical Language System. Methods Arch. 1993;32(4): 281-291.

[6]   Rahman M, Antani SK, Thoma GR, U.S.N. Library. A Medical Image Retrieval Framework in Correlation Enhanced Visual Concept Feature Space. Proc. 22nd IEEE International Symposium on Computer-Based Medical Systems, Albuquerque, NM, April 2009: pp. 6–9.

[7]   Thoma GR. A Classification-Driven Similarity Matching Framework for Retrieval of Biomedical Images. Proc. ACM International Conference on Multimedia Information Retrieval. March 2010: pp. 147-154.

[8]   Xue Y, Cheng T, Xu X, Gao Z, Li Q, Liu X, Wang X, Song R, Ju X, Zhang Q. "High-Accuracy and Real-Time 3D Positioning, Tracking System for Medical Imaging Applications based on 3D Digital Image Correlation. Opt. Lasers Eng. 2017;88:82–90.

[9]   Zhang S, Metaxas D. Large-Scale Medical Image Analytics: Recent Methodologies, Applications and Future Directions. Med. Image Anal. 2016;33:98–101.

[10]   Sundarapandian M, Kalpathi R, Siochi RAC, Kadam AS. Lung Diaphragm Tracking in CBCT Images Using Spatio-Temporal MRF. Comput. Med. Imaging Graph., 2016;53:9–18.

[11]   Bright TJ, Wong A, Dhurjati R, Bristow E, Bastian L, Coeytaux RR, Samsa G, Hasselblad V, Williams JW, Musty MD, Wing L, Kendrick AS, G. D. Sanders, and D. Lobach, "Annals of Internal Medicine Review Effect of Clinical Decision-Support Systems," *Ann. Intern. Med.*, vol. 157, no. 1, pp. 29–43, 2012.

[12]   Zhang D, Wong A, Indrawan M, Lu G. Content-Based Image Retrieval Using Gabor Texture Features. Proc. IEEE Pacific-Rim Conference on Multimedia, University of Sydney, Australia. 2000: pp. 392-395.

[13]   Ghosh S, Ghosh A. Content Based Retrieval of Malaria Positive Images from a Clinical Database via Recognition in RGB Colour Space. Proc. 48th Annual Convention of Computer Society of India-Vol II: *ICT and Critical Infrastructure: S*pringer International Publishing. 2014: pp. 1-8.

[14]   Bugatti PH, Kaster DS, Ponciano-Silva M, Traina C, Azevedo-Marques PM, Traina AJM. Prosper: Perceptual Similarity Queries in Medical CBIR Systems Through User Profiles. Comput. Biol. Med. 2014;45(1):8–19.

[15] Hruby GW, Rasmussen LV, Hanauer D, Patel VL, Cimino JJ, Weng C. A Multi-Site Cognitive Task Analysis for Biomedical Query Mediation, Int. J. Med. Inform. 2016;93:74–84.

[16] Istephan S, Siadat MR. Unstructured medical image query using big data - An epilepsy case study. J. Biomed. Inform. 2016;59:218–226.

[17] Tramontana E. Graphic object feature extraction system based on cuckoo search algorithm. Expert Systems with Applications. 2016;66:20-31.

[18] Behrisch M, Bach B, Hund M, Delz M, von Ruden L, Fekete J-D, Schreck T. Magnostics: Image-based Search of Interesting Matrix Views for Guided Network Exploration. IEEE Trans. Vis. Comput. Graph. 2016;2626(c):1-1.

[19] Zhang F, Song Y, Cai W, Liu S, Pujol S, Kikinis R, Xia Y, Fulham M, Feng D. Pairwise latent semantic association for similarity computation in medical imaging. IEEE Trans Biomed Eng. Sept. 10, 2015. DOI: 10.1109/TBME.2015.2478028.

[20] Hiremath PS, Pujari J. Content Based Image Retrieval Using Color, Texture and Shape Features. Proc. 2012 18th Int. Conf. Adv. Comput. Commun., 2007: vol. 0, pp. 780–784.

[21] Yuan H, Zhang X. Texture Image Retrieval Based on a Gaussian Mixture Model and Similarity Measure Using a Kullback Divergence. Proc. IEEE International Conference on Multimedia and Expo (ICME), 2004: pp. 1867–1870.

[22] Jalaja K, Bhagvati C, Deekshatulu BL, Pujari AK. Texture Element Feature Characterizations for CBIR. Proc. IEEE Geoscience & Remote Sensing Symposium. 2005: vol. 500046, pp. 733–736.

[23] Mohapatra P, Chakravarty S, Dash PK. An improved cuckoo search based extreme learning machine for medical data classification. Swarm Evol. Comput. 2015;24:25–49.

[24] Oh H-S, Jung Y. Cluster-based query expansion using external collections in medical information retrieval. J. Biomed. Inform. 2015;58:70–79.

[25] Szlosek DA, Ferretti JM. Using Machine Learning and Natural Language Processing Algorithms to Automate the Evaluation of Clinical Decision Support in Electronic Medical Record Systems. eGEMs (Generating Evidence & Methods to improve patient outcomes). 2016;4(3), DOI: http://dx.doi.org/10.13063/2327-9214.1222.

[26] Zalis M, Harris M. Advanced Search of the Electronic Medical Record: Augmenting Safety and Efficiency in Radiology. J. Am. Coll. Radiol. 2010;7(8):625–633.

[27] Marco-Ruiz L, Pedrinaci C, Maldonado JA, Panziera L, Chen R, Bellika JG. Publication, discovery and interoperability of Clinical Decision Support Systems: A Linked Data approach. J. Biomed. Inform. 2016;62:243–264.

[28] Molenbruch Y, Braekers K, Caris A, Vanden Berghe G. Multi-directional local search for a bi-objective dial-a-ride problem in patient transportation. Comput. Oper. Res. 2017;77: 58–71.

[29] Redd AM, Gundlapalli AV, Divita G, Carter ME, Tran L-T, Samore MH. A Pilot Study of a Heuristic Algorithm for Novel Template Identification from {VA} Electronic Medical Record Text. J. Biomed. Inform. 2016; doi: 10.1016/j.jbi.2016.07.019.

[30] Jiang J, Zheng J, Zhao C, Su J, Guan Y, Yu Q. Clinical-decision support based on medical literature: A complex network approach. Phys. A Stat. Mech. its Appl. 2016;459:42–54.

[31] Liu X, Huang L, Deng C, Lang B, Tao D. Query-Adaptive Hash Code Ranking for Large- Scale Multi-View Visual Search. 2016;25(10):4514–4524.

[32] Mourão A, Martins F, Magalhães J. Multimodal medical information retrieval with unsupervised rank fusion.

Comput. Med. Imaging Graph. 2015;39:35–45.

[33] Demner-Fushman D, Antani S, Thoma GR. Automatically Finding Images for Clinical Decision Support. Proc. 7th IEEE International Conference on Data Mining (ICDM 2007), Omaha, NE, October 28-31, 2007: pp. 139–144.

[34] Demner-Fushman D, Antani S, Simpson M, Thoma GR. Annotation and retrieval of clinically relevant images. Int J Med Inform. 2010;78(12):1–18.

[35] Agrawal JP, Erickson, Kahn, Jr CE. Imaging informatics: 25 years of progress. IMIA Yearbook of Medical Informatics 2016. http://imia.shattauer.de

[36] Peterson CW, Rose D, Mink J, Levitz. Real-time monitoring and evaluation of a visual-based cervical cancer screening program using a decision support job aid. Diagnostics 2016, (6) 20:1-8.

[37] De Silva T, et al. Utility of the LevelCheck algorithm for decision support in vertebral location. Spine 2016. Online copy available ahead of print. DOI: 10.1097/BRS.0000000000001589

[38] Antani SK, You D, Simpson M, Rahman M, Demner-Fushman D, Thoma GR. The role of image modality and visual characteristics in archiving biomedical images. Proc of IS&T Archiving Conference. Volume 2013, Number 1, 2013: pp. 31-35.

[39] Rahman MM, You D, Simpson M. An interactive image retrieval framework for biomedical articles based on visual region-of-interest (ROI) identification and classification [Abstract]. The 2nd IEEE Conference on Healthcare Informatics, Imaging, and Systems Biology Analyzing Big Data for Healthcare and Biomedical Sciences (HISB 2012). La Jolla, CA. September 2012.

[40] Simpson MD, You D, Rahman MM, Xue Z, Demner-Fushman D, Antani S, Thoma G. Literature-based biomedical image classification and retrieval.

Computerized Medical Imaging and Graphics. 2015;39:3-13.

[41] Kalpathy-Cramer J, García Seco de Herra A, Demner-Fushman D, Antani S, Bedrick S, Müller H. Evaluating performance of biomedical image retrieval systems—an overview of the medical image retrieval task at ImageCLEF 2004-2013. Computerized Medical Imaging and Graphics. 2015;39:55-61.

[42] Vajda S. Label the many with a few: Semi-automatic medical image modality discovery in a large image collection. Proc. IEEE Symposium Series on Computational Intelligence. Orlando, FL, Dec 9-12, 2014

[43] Xue Z, Rahman MM, Antani S, Long LR, Demner-Fushman D, Thoma GR. Modality classification for searching figures in biomedical literature. Proc. 29th IEEE International Symposium on Computer-Based Medical Systems. Dublin and Belfast, June 2016.

[44] Xue Z, You D, Chachra S, Antani SK, Long LR, Demner-Fushman D, Thoma GR. Extraction of endoscopic images for biomedical figure classification. Proc. SPIE. 9418, Medical Imaging 2015: PACS and Imaging Informatics: Next Generation and Innovations, 94180P. (March 17, 2015) doi: 10.1117/12.2081033.

[45] Xue Z, You D, Antani SK, Long LR, Demner-Fushman D, Thoma GR. Classification of Visual Signs in Abdominal CT Image Figures in Biomedical Literature. Proc. SPIE. 9039. Medical Imaging 2014: PACS and Imaging Informatics: Next Generation and Innovations. 90390T.

[46] Xue Z, You D, Candemir S, Jaeger S, Antani SK, Long LR, Thoma GR. Chest X-ray Image View Classification. Proc. 28th IEEE International Symposium on Computer-Based Medical Systems. Sao Carlos, SP, Brazil. February 2015.

[47] Xue Z, Antani SK, Long LR, Demner-Fushman D, Thoma GR. Body Segment

Classification for Visible Human Cross Section Slices. IEEE 27th International Symposium on Computer-Based Medical Systems (CBMS), New York, NY, May 2014: pp. 199-204

[48] You D, Simpson M, Antani SK, Demner-Fushman D, Thoma GR. A robust pointer segmentation in biomedical images toward building a visual ontology for biomedical article retrieval. Proc. SPIE 8658, Document Recognition and Retrieval XX, 86580Q (February 4, 2013); doi:10.1117/12.2005934.

[49] You D, Rahman MM, Antani SK, Demner-Fushman D, Thoma GR. Text- and content-based biomedical image modality classification. Proc. SPIE Medical Imaging. Orlando, FL. February 2013;8674-21.

[50] You D, Simpson M, Antani SK, Demner-Fushman D, Thoma GR. Annotating image ROIs with text descriptions for multimodal biomedical document retrieval. Proc. SPIE 8658, Document Recognition and Retrieval XX, 86580Q (February 4, 2013); doi:10.1117/12.2005934; http://dx.doi.org/10.1117/12.2005934.

[51] You D, Antani SK, Demner-Fushman D, Thoma GR. Does Figure-Text Improve Biomedical Article Retrieval? A Pilot Study. Proc. of Computer-based Medical Systems. New York, NY, CBMS 2014. May 2014.

[52] http://imageclef.org/2010/medical. Last accessed September 25, 2016.

[53] Faingold R, Daneman A, Tomlinson G, et al. Necrotizing enterocolitis: Assessment of bowel viability with color Doppler US. Radiology 2005;235:587-594.

[54] Restrepo C S, Diethelm L, Lemos J A, et al. Cardiovascular complications of human immunodeficiency virus infection. RadioGraphics 2006;26:213-231.

[55] Talianovic M S, Hunter T B, Miller M D, et al. Gallery of medical devices. RadioGraphics 2005;25:859-870.

[56] Hiller N, Lieberman S, Chajek-Shaul T, et al. Thoracic manifestations of Behçet disease at CT. RadioGraphics 2004;24:801-808.

[57] Clark H P, Carson W F, Kavanagh P V, et al. Staging and current treatment of hepatocellular carcinoma. RadioGraphics 2005;25:S3-S23.

[58] Awai K, Murao K, Ozawa A, et al. Pulmonary nodules at chest CT: Effect of computer-aided diagnosis on radiologists' detection performance. Radiology 2004;230:347-352.

[59] Blum A G, Zabel J-P, Kohlmann R, et al. Pathologic conditions of the hypothenar eminence: Evaluation with multidetector CT and MR imaging. RadioGraphics 2006;26:1021-1044.

[60] Rhim H, Dodd G D, Chintapalli K N, et al. Radiofrequency thermal ablation of abdominal tumors: Lessons learned from complications. RadioGraphics 2004;24:41-52.

[61] Pickhardt P J. Differential diagnosis of polypoid lesions seen at CT colonography (virtual colonoscopy). RadioGraphics 2004;24:1535-1556.

[62] Prasad S R, Wang H, Rosas H, et al. Fat-containing lesions of the liver: Radiologic-pathologic correlation. RadioGraphics 2005;25:321-331.

[63] Bos C, Delmas Y, Desmoulière A, et al. In vivo MR imaging of intravascularly injected magnetically labeled mesenchymal stem cells in rat kidney and liver. Radiology 2004;233:781-789.

[64] Berrocal T, Parrón M, Alvarez-Luque A, et al. Pediatric liver transplantation: A pictorial essay of early and late complications. RadioGraphics 2006;26:1187-1209.

[65] Levy A D, Patel N, Dow N, et al. Abdominal neoplasms in patients with neurofibromatosis type 1: Radiologic-pathologic correlation. RadioGraphics 2005;25:455-480.

[66] Wittram C , Maher M M, Yoo A J, et al. CT angiography of pulmonary embolism: Diagnostic criteria and

causes of misdiagnosis. RadioGraphics 2004;24:1219-1238.

[67]   Stanley RJ, Stoecker WV, Moss RH, Rabinovitz HS, Armand B, Argenziano G, Soyer HP. A basis function feature-based approach for skin lesion discrimination in dermatology dermoscopy images. Skin Research and Technology. 2011;14(4):425–435.

[68]   Nourbakhsh F, Pati PB, Ramakrishnan AG. Text Localization and Extraction from Complex Gray Images. Proc. Indian Conf. Vision, Graphics Image Processing, ICVGIP. Dec. 13-16, 2006: pp. 776-785.

[69]   Jalab HA. Image retrieval system based on color layout descriptor and Gabor filters. Proc. IEEE Conference on Open Systems (ICOS2011). Langkawi, Malaysia. Sept. 25-28, 2011: pp. 32-36. http://people.csail.mit.edu/torralba/code/ spatialenvelope/. Last accessed on September 16, 2016.

[70]   Oliva A, Torralba A. Modeling the shape of the scene: a holistic representation of the spatial envelope. International Journal of Computer Vision. 2001;42(3):145-175.